International Journal of Coal Geology 306 (2025) 104793

Contents lists available at ScienceDirect

International Journal of Coal Geology

journal homepage: www.elsevier.com/locate/coal

Relating systematic molecular and textural properties of graptolite pyrolyzed via gold tube hydrous pyrolysis: Implications for thermal proxies in lower Paleozoic marine shales☆

Xiaowei Zheng [a,b], Hamed Sanei [c], Fujie Jiang [a,b,**], Qingyong Luo [a,b], Ye Wang [d], Jennifer L. Nedzweckas [e], Brett J. Valentine [e], M. Rebecca Stokes [e], Liu Cao [a,b], Paul C. Hackley [e,*]

[a] National Key Laboratory of Petroleum Resources and Engineering, China University of Petroleum, Beijing 102249, China
[b] College of Geosciences, China University of Petroleum, Beijing 102249, China
[c] Lithospheric Organic Carbon (LOC) Group, Department of Geoscience, Aarhus University, 8000, Denmark
[d] School of Earth Science and Resources, Key Laboratory of Western Mineral Resources and Geological Engineering of Ministry of Education, Chang'an University, Xi'an 710054, China
[e] U.S. Geological Survey, MS 954 National Center, 12201 Sunrise Valley Dr, Reston, VA 20192, USA

ARTICLE INFO

Keywords:
Graptolite
Lower Paleozoic shale
Thermal maturity
Raman spectroscopy
Organic petrology

ABSTRACT

A series of gold tube pyrolysis experiments (72 h, 300–550 °C, 50 MPa) conducted on a graptolite-rich lower Paleozoic marine shale generated pyrolysis residues for a comprehensive evaluation of the molecular and structural variability of three types of graptolite periderm. Organic petrology, Raman spectroscopy, and field emission scanning electron microscopy (FE-SEM) with energy dispersive spectroscopy (EDS) were combined to evaluate the thermal evolution process. The three types of graptolite periderm, namely granular, non-granular, and nodular graptolite, were analyzed by Raman spectroscopy wherein point measurements were obtained after the maceral was identified and the location verified by organic petrology. Distinct thermal evolution pathways among non-granular, granular, and nodular graptolite periderms were recorded. The evolution patterns of the Raman parameters, particularly D1 and G bands, highlight the differences in geochemical composition of the graptolite periderm types and the alteration of molecular structure with increasing thermal maturity. Raman parameters D1 (position of the D1 peak), G-FWHM (full width at half maximum of the G peak), and ratios D1-FWHM/G-FWHM (full width at half maximum of the D1 peak ratioed to G-FWHM) and A_{D1}/A_G (ratio of D1 and G peak intensities) showed effectiveness in assessing thermal maturity. Bireflectance with increasing gold tube pyrolysis temperature followed a hierarchy: non-granular > granular > nodular, reflecting different molecular alignment intensities. Qualitative FE-SEM evaluation showed that fine-grained mineral inclusions (primarily Fe-sulfide as determined via EDS) were associated with the graptolite populations, with granular graptolite containing greater amounts of coarser-grained (e.g., ~300–1400 nm) mineral inclusions relative to non-granular and nodular graptolite, which contain finer-grained (e.g., ~100–200 nm) inclusions difficult to resolve with optical microscopy. These findings are investigated to highlight the mechanisms that drive organic matter evolution within graptolite during thermal maturation, as well as to explore some of the limitations of using spectroscopic parameters as thermal maturity proxies.

1. Introduction

Vitrinite is very sensitive to the determination of the maturity of kerogen in terrestrial sedimentary strata (coal-lacustrine) (International Committee for Coal Petrology (ICCP, 1998). However, primary vitrinite does not occur in aquatic sedimentary strata (marine) (Goodarzi et al.,

☆ This article is part of a Special issue entitled: 'TSOP 2024' published in International Journal of Coal Geology.

* Corresponding author at: U.S. Geological Survey, MS 954 National Center, 12201 Sunrise Valley Dr, Reston, VA 20192, USA.
** Corresponding author at: National Key Laboratory of Petroleum Resources and Engineering, China University of Petroleum, Beijing 102249, China.
E-mail addresses: jiangfj@cup.edu.cn (F. Jiang), phackley@usgs.gov (P.C. Hackley).

https://doi.org/10.1016/j.coal.2025.104793
Received 12 February 2025; Received in revised form 16 April 2025; Accepted 5 May 2025
Available online 6 May 2025

2022), and the lower Paleozoic and older sedimentary strata, therefore alternative thermal maturity indices, e.g., programmed pyrolysis T_{max}, biomarker isomerization, Raman spectroscopy, reflectance of vitrinite-like particles, zooclasts, and solid bitumen have been applied for thermal maturity evaluation (Goodarzi and Norford, 1987; Suárez-Ruiz et al., 2012; Petersen et al., 2013; Goodarzi et al., 2024a). Among these thermal maturity indices, graptolite reflectance (GR_o) has received great attention due to its sensitivity to thermal stress and its origin as a primary organic maceral with a distinct biological precursor (Goodarzi, 1984; Bustin et al., 1989). However, recent work found that there are different anatomical fractions of graptolite showing different organic geochemical compositions with distinct hydrocarbon generation potential and optical characteristics (Zheng et al., 2021). In addition, the evolution of graptolite reflectance via petrographic evaluation of gold tube pyrolysis products showed an anomalous breakdown in the correlation of GR_o versus thermal maturity (Zheng et al., 2022). This anomalous trend is characterized as a suppressed GR_o gradient throughout the entire gas window (VR_o: 1.0–2.0 %, Mukhopadhyay, 1994). Beyond 2.0 %, GR_o resumes its increasing trend with a similar gradient as the pre-gas window, due to continued aromatization and condensation of the graptolite organic structure (Goodarzi et al., 2024).

Raman spectroscopy, a non-destructive and rapid microstructural analysis technique, has recently emerged as a powerful tool for assessing the thermal maturity of source rocks (Hackley and Lünsdorf, 2018; Henry et al., 2018; Kelemen and Fang, 2001; Ferralis et al., 2016; Jubb et al., 2018). Various bands (or peaks) in the Raman spectrum correspond to different vibrational modes of the molecules, which provides information about the molecular structure, chemical composition, and physical properties. For example, the G band (~1600 cm^{-1}), indicative of well-ordered graphite-like carbon structures, and the D band (~1350 cm^{-1}), associated with lattice defects in the sp^2 carbon network (Tuinstra and Koenig, 1970; Marshall et al., 2012; Beyssac et al., 2002), are widely used for thermal maturity evaluation (Henry et al., 2019; Sauerer et al., 2017). Studies have revealed several maturity indicators, e.g., D and G peak positions, full width at half maximum (FWHM), intensity ratios (D1/G), and Raman band separation (RBS) between D1 and G bands (Kelemen and Fang, 2001). Applicability of these Raman thermal proxies has been extended to various OM types, such as vitrinite, solid bitumen, and graptolites, by correlating the Raman spectral parameters with traditional thermal maturity proxies, such as reflectance and programmed pyrolysis T_{max} (Liu et al., 2013; Wilkins et al., 2014; Jubb et al., 2018; Morga and Pawlyta, 2018), and has thus proven to be useful in determining thermal maturity. In addition, data from different studies might be discrepant, as the influence of sample types (natural or artificially matured), laser excitation wavelength, and spectral deconvolution procedures all influence the parameters obtained (Mumm and İnan, 2016; Sauerer et al., 2017; Henry et al., 2019). As there is no standardized approach in using Raman spectroscopy to determining thermal maturity, it will be useful to test the effects of different heating rates, pressures and deformation styles from experiments to get a better appreciation of how different environments and physiochemical difference may impact the Raman spectrum (Henry et al., 2019).

Raman spectroscopic character of graptolite has not been determined for the individual anatomical fractions, hence lacking the systematic understanding of the morphological and textural evolution of graptolite. Hence, to improve accuracy in the application of reflectance or Raman spectral analysis of graptolite, this work aims to demonstrate the mechanism behind the apparent thermal variation of graptolite reflectance by combining morphological and molecular structural information. Advanced understanding of these thermal maturity proxies can have significant geological importance for accurate determination of thermal maturity and basin modelling in pre-Devonian sedimentary basins.

2. Samples and methodology

A Lower Ordovician Tremadocian graptolite-rich Alum Shale core sample collected from Estonia was artificially matured by gold tube pyrolysis to generate a series of pyrolyzed residue samples with different maturity levels. The organic matter composition of the original sample includes alginite, liptoderinite, bituminite, solid bitumen, vitrinite-like, and graptolite. Some results from the pyrolyzed samples have been previously published, including gas content and stable isotopes (Zheng et al., 2021) and a detailed graptolite reflectance study of the solid residues (Zheng et al., 2022). In this work, the same sample series was further studied by using high resolution field emission scanning electron microscopy (FE-SEM) and Raman spectroscopy to record textural and chemical evolution of graptolite periderm during important hydrocarbon generation stages. Correlative Raman spectroscopy and FE-SEM point data were collected by systematically relocating the same areas on the samples (e.g., Stokes et al., 2022).

2.1. Gold tube hydrous pyrolysis

The gold tube pyrolysis experiments were conducted in the State Key Laboratory of Petroleum Resources and Prospecting, China University of Petroleum-Beijing. The original immature core sample (crushed and sieved to the size range of 1.5–2.5 mm) was loaded into gold tubes vessel (length 40 mm and inner diameter 5.5 mm and 0.25 mm in thickness), together with isovolumetric deionized water, and sealed under an argon atmosphere. The isothermal pyrolysis temperatures were from 300 to 550 °C for 72 h under a hydrostatic pressure of 50 MPa in the furnace (Jin et al., 2021; Wu et al., 2021). Sweeney and Burnham (1990) presented a simplified vitrinite maturation model, called EASY%Ro, by employing an Arrhenius first-order parallel reaction framework with distributed activation energies, calibrated against coal vitrinite chemical properties. It has been widely applied in the petroleum geology industry. The model enables prediction of vitrinite reflectance evolution (0.3–4.5 % Ro) across laboratory to geological timescales (1 °C/week to 1 °C/10 Myr) and facilitates thermal history optimization by generating reflectance-depth profiles for comparison with borehole data. Hence, the corresponding EASY%Ro values from the gold tube hydrous pyrolysis in this work was calculated to be from 0.59 % to 4.67 % (Table 1). The graptolite reflectance of the individual anatomical components was measured in previous work (Zheng et al., 2022) and is reproduced in Table 1. Multiple aliquots of a single coal sample (Permian, Shanxi Formation, China) were used in a parallel set of gold tube experiments and were analyzed with vitrinite reflectance increasing from 0.75 % to 3.32 % (Zheng et al., 2022).

2.2. Organic petrology

A detailed organic petrology study was conducted on the samples in the Lithospheric Organic Carbon (LOC) laboratory, Aarhus University, and the data of maceral identification, random reflectance measurement and fluorescence spectrum could be found in previous works (Zheng et al., 2021; Zheng et al., 2022). Polarized light was used to measure the GRmax and GRmin (maximum GR and minimum GR). The same samples were observed with white light, grayscale, and blue light fluorescence, and maps of the sample surfaces were created to aid navigation among different fragments of graptolite (i.e., granular, non-granular, nodular), and to guide subsequent Raman and FE-SEM analysis at the U.S. Geological Survey (USGS) (e.g., Valentine et al., 2019).

2.3. Raman microscopy

Spectra were collected on a Horiba Xplora Plus Raman microscope system at the USGS Raman Spectroscopy Lab in Reston, VA. The setting of experimental parameters included a 532 nm laser with perpendicular polarization, 1200 groove/mm spectral grating, 300 μm confocal

Table 1
The pyrolysis temperature, EASY%Ro, VR_o in the corresponding coal and reflectance of the three fractions of graptolite (Zheng et al., 2022).

Sample ID	Gold tube temperature	Duration	EASY%Ro	VR_o in coal	GR_o, nodular			GR_o, NGG			GR_o, GG		
# No.	°C	hrs	%	%	mean	SD	n	mean	SD	n	mean	SD	n
EST3008					0.58	0.06	34	0.68	0.05	103	0.49	0.07	114
2–3	300	72	0.71	0.75	0.92	0.09	21	0.96	0.10	107	0.62	0.11	64
2–4	325	72	0.85	0.99	1.24	0.09	30	1.33	0.19	100	0.75	0.13	45
2–6	370	72	1.32	1.25	1.45	0.08	29	1.46	0.13	81	0.89	0.11	36
2–7	390	72	1.54	1.53	1.59	0.08	29	1.55	0.14	82	1.02	0.15	45
2–8	400	72	1.75	1.73	1.65	0.10	20	1.60	0.17	82	1.11	0.17	56
2–9	415	72	2.00	2.03	1.99	0.10	30	1.86	0.17	71	1.35	0.15	49
2–11	470	72	3.07	2.41	2.41	0.10	38	2.19	0.18	79	1.53	0.22	34
2–12	500	72	3.64	2.94	2.89	0.11	27	2.84	0.37	132	2.00	0.29	67
2–13	550	72	4.35	3.32	3.22	0.13	32	3.44	0.40	68	2.29	0.35	50

VR_o—mean random vitrinite reflectance; GR_o—mean random graptolite reflectance; NGG—non-granular graptolite; GG—granular graptolite; Nodular—nodular graptolite; SD—standard deviation; n—number of measurements.

pinhole diameter, 100 μm spectrometer slit, with ~75 μW laser power delivered at the sample surface through a 100× objective with a numerical aperture of 0.9. Each analysis was collected across a spectral range of 109–2706 cm^{-1} in three accumulations of 12 to 15 s. The laser spot size was conservatively estimated to be 1 μm in diameter at the sample surface and the measurement locations were checked post-analysis to ensure that no damage occurred from the laser. Spectra were fit across a range of 800–2000 cm^{-1} using a linear background function and a sum of five Lorentzian peak functions representing the D4, D1, D3, D2 and G peaks (Wu et al., 2022, Fig. 1). All USGS-generated Raman spectroscopy data generated for this work are compiled in tables in this manuscript and available online from Zheng et al. (2025).

2.4. FE-SEM

Subsequent to organic petrography and Raman spectroscopy, 4 samples (2–3, 2–4, 2–6, 2–9 and 2–11, with EASY%Ro values of 0.71 %, 0.85 %, 1.32 %, 2.00 % and 3.07 %, respectively) were selected to represent the transition across the oil and gas windows. These samples were prepared with a Technoorg Linda SEMPrep 2 argon broad ion beam mill and analyzed using a Hitachi SU5000 variable pressure FE-SEM at the USGS in Reston to document and observe surface features that may contribute to anomalous reflectance within graptolites. The samples were first ion milled (6 kV; 2.5 mA; 3degree angle; 4 rpm rot.; 30 min.) to make a flatter surface for improved surface characterization by FE-SEM. A conductive sputter coating of iridium (3 nm) was applied to the pellet surfaces to reduce beam damage and to improve image resolution. FE-SEM (10 keV; 30 spot intensity) was conducted under high vacuum conditions (<$1.0E^{-3}$ Pa in the sample chamber) and low working distance (3 mm) to improve spatial resolution, with some areas further imaged under backscattered electrons (BSE, working distance 5 mm) to better show contrast of the minerals within the organic-rich matrices. Energy dispersive spectroscopy (EDS) to assess mineral characterization and elemental mapping of graptolites was completed using an Oxford Ultim Plus EDS detector (20 keV, 50 spot intensity, at a working distance of 10 mm).

3. Results

3.1. Organic petrology of three types of graptolite periderm

Three fractions of graptolite periderm: (i) non-granular graptolite (NGG), (ii) granular graptolite (GG), and (iii) nodular graptolite, were identified among samples across the whole maturation process (from natural immature sample until EASY%Ro of 4.35 %, Fig. 2). The typical (i) non-granular graptolite has a distinct lath-shape with sharp edges, and a smooth reflecting surface. Riediger et al. (1989) recognized two varieties of non-granular graptolite: Blocky fragments and lath-shaped

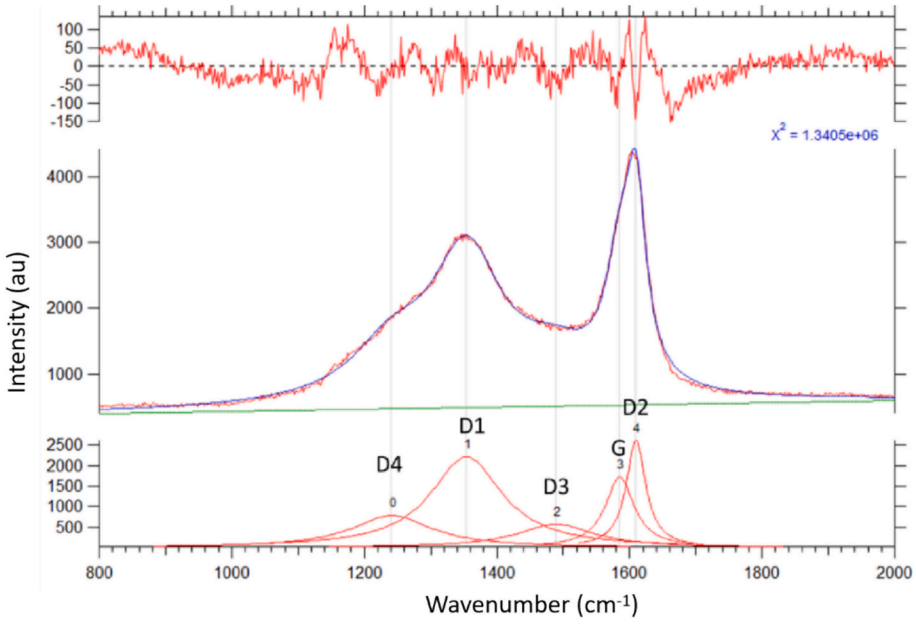

Fig. 1. Example of the five-peak Lorentzian fitting function applied for the spectral deconvolution procedure in this work.

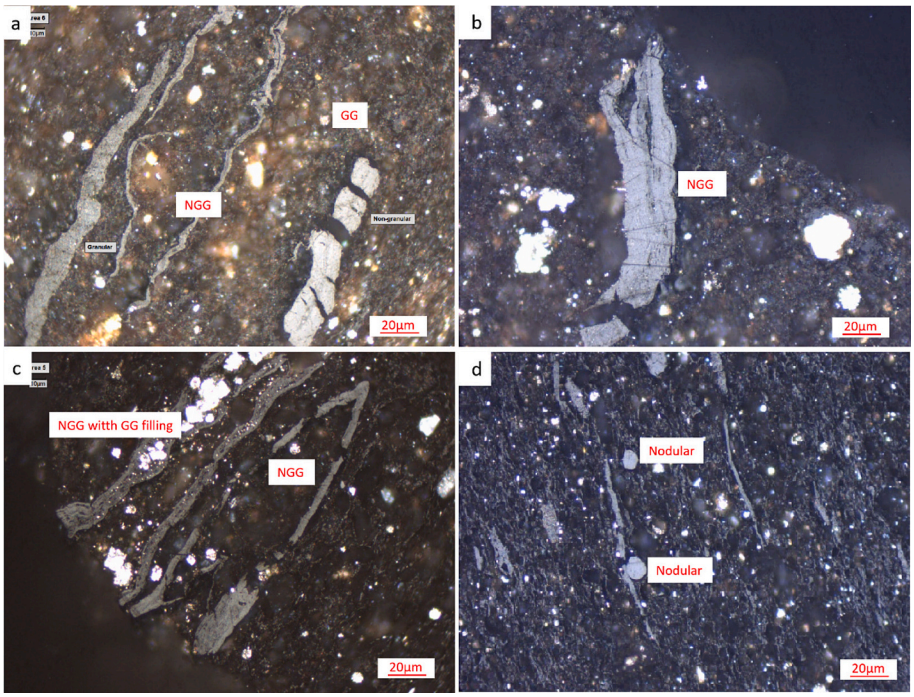

Fig. 2. Photomicrographs of pyrolyzed granular graptolite and non-granular graptolite: a) and b) Artificially matured sample at a pyrolysis temperature of 300 °C with EASY%Ro of 0.71 %; c) at a pyrolysis temperature of 325 °C with EASY%Ro of 0.99 %; d) at a pyrolysis temperature of 370 °C with EASY%Ro of 1.32 %. NGG—non-granular graptolite; GG—granular graptolite; Nodular—nodular graptolite.

fragments. It is blocky in sections parallel to bedding, but may display a long stipe-like morphology in sections normal to bedding (Link et al., 1990)). The (ii) granular graptolite co-occurs with (i) non-granular graptolite as a well-preserved binary biostructure (i.e., a granular infilling), or occurs alone as an independent structureless fragment (Zheng et al., 2022), the latter of which is commonly found associated with mineral particles (Ma et al., 2016). The granular graptolite fragments have an angular blocky shape and are distinguished by their finely granular to reticular texture and they may represent the remains of the soft-bodied part of the graptolite organism that occupied the common canal (Goodarzi, 1984). The (iii) nodular graptolite has a solid round shape, demonstrating that it is a primary maceral without migration ability, i.e., is not solid bitumen.It is noteworthy when identifying NGG from chitinozoan as Ro values for chitinozoans and

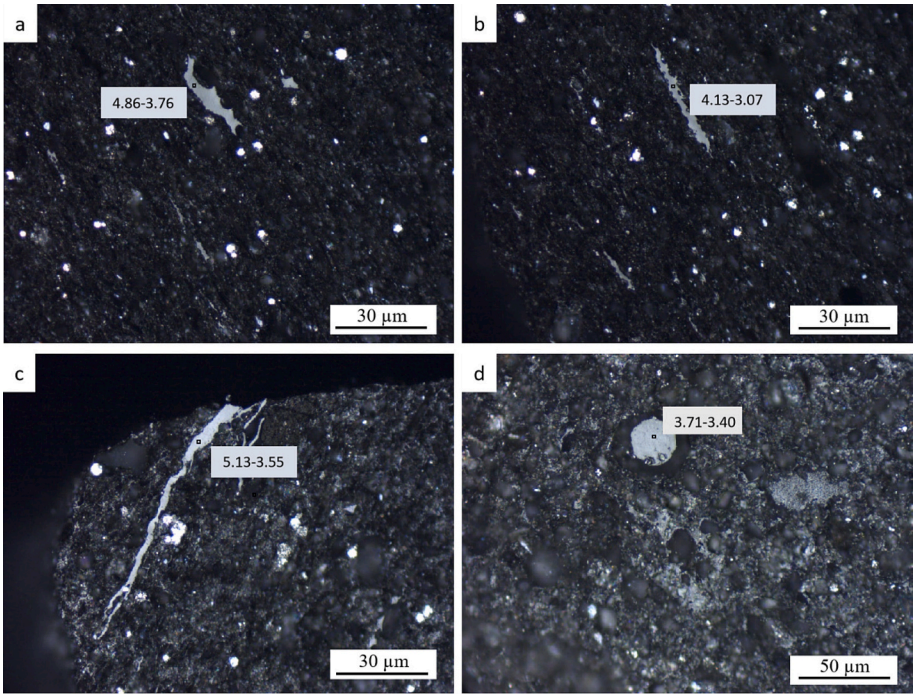

Fig. 3. Photomicrographs of graptolite under polarized light, the marked reflectance are GRmax and GRmin separately: (a and b) Anisotropy of non-granular graptolite after hydrous pyrolysis at 500 °C and (c) 550 °C. (d) Isotropy of granular graptolite after hydrous pyrolysis at 550 °C.

graptolites are close to each other throughout pyrolysis (Reyes et al., 2018). Chitinozoans exhibit a bottle-shaped test, featuring an oral tube and ornamented chamber; While graptolite has unique fusellar architecture under thin cortical layers (Bertrand, 1990). The fusellar structure is easy to observe in transmitted light when cortical tissue are thin, while graptolite can be recognized by their finely laminated structure (reflected light) and a vitrinite-like color when cortical tissues are thick (Goodarzi, 1984). The thermal maturation of graptolites proceeds through structural reorganization phases, characterized by increasing GRo (Fig. S1) as aromatic condensation and graphitic ordering (Goodarzi and Murchison, 1972; Teichmüller and Teichmüller, 1979). Polarized light was applied and the graptolite showing stronger anisotropy in high maturity samples (Fig. 3a, b, c). Anisotropy were observed in non-granular and granular graptolites, which is in accordance with the observation from Goodarzi (1985), Goodarzi and Norford (1987) and Luo et al. (2018). Systematic reflectance anisotropy (GRomax vs. GRor) demonstrate the critical influence of bedding orientation and thermal history on optical properties of graptolite (Goodarzi, 1985; Luo et al., 2017, 2018). However, nodular graptolite is isotropic (Fig. 3d).

3.2. Raman spectra evolution with thermal maturation

Raman spectral parameters from the three types of graptolite periderm (non-granular, granular, nodular) are listed in Table 2. In general, D4 band, D1 band and D2 band peaks shift to lower wavenumbers as thermal maturity increases (Table 2, Fig. 3a, c, i). The D1 peak position evolves from wavenumber 1368 cm^{-1} down to 1354 cm^{-1} with GR_o values up to about 1.5 %, then plateaus up to GR_o values of about 2.0 %, after which it decreases again (Fig. 3c). The D2 peak position (from 1307 cm^{-1} to 1236 cm^{-1}) and D4 peak position (from 1614 to 1610 cm^{-1}) diminish until a GR_o value of about 1.5 % and then plateau at higher GR_o. In contrast, the peak intensity of the D3 (between 1458 and 1490 cm^{-1}) and G peaks (between 1575 and 1585 cm^{-1}) shift toward higher wavenumber with increasing GR_o. The FWHM of all peaks, except D1, decrease up to GR_o of about 1.5 % and gradually decrease with lower rate at higher GR_o values. Finally, the FWHM of D1 keeps increasing as GR_o increase (Fig. 3b, d, f, h, j).

The relationship between reflectance of the three graptolite types and their Raman parameters reveals the textural and aromatic evolution of graptolite during thermal maturation (Fig. 4). The three types of graptolite periderm have distinct evolution trends, with the peak position and FWHM of D4 and G exhibiting the clearest and most stable trends in general, whereas the same peak parameters from the nodular graptolite population tend to have a less systematic relationship to GR_o (Fig. 4a, b, g, h). The peak position of D1 and D2-FWHM of the three graptolite types and D1-FWHM of granular and non-granular graptolite show a decreasing tendency with increasing thermal maturity, suggesting increasing disorder (higher D1-FWHM), while the overall aromaticity increases (decreasing G-FWHM) (Fig. 4d, h). This illustrates the varied aromatic characteristics of the three graptolite fractions during thermal evolution, with potential implications for determination of thermal maturity dependent on which graptolite fraction is measured.

3.3. Surface features of graptolite periderm with thermal maturation

Based on FE-SEM evaluation, ion milling artifacts found in the graptolites include sputter-induced voids, tracks, and curtains. Tracks are linear nanometer-scale scratches mainly found in softer OM, occurring in concave recesses. Curtains, also known as the waterfall effect, are parallel elongated ridges and channels that develop across various materials, especially at boundaries with contrasting compositions (Valentine and Hackley, 2023).Fig. 4 shows the development of uniform and isolated nm-scale ion-induced artifacts which are different in character from naturally developed organic pores, which typically exhibit irregular sizes/shapes and are connected with adjacent pores structures (Valentine and Hackley, 2023). Graptolites tended to have a higher secondary electron (SE) signal (brighter) compared to other OM

Table 2
Raman spectral parameters of the pyrolyzed samples for the three types of graptolites.

# No	Graptolite type	n	*D1-peak position* (cm^{-1})	SD (cm^{-1})	*G-peak position* (cm^{-1})	SD (cm^{-1})	*G-FWHM* (cm^{-1})	SD (cm^{-1})	$D1_{FWHM}/G_{FWHM}$	A_{D1}/A_G
	granular	4	1367	1.40	1577	0.55	76.16	1.44	1.28	0.61
	nodular	3	1364	0.89	1576	5.46	87.49	2.36	1.41	0.72
EST3008	non-granular	3	1368	0.79	1578	0.58	77.44	1.15	1.25	0.58
	granular	5	1367	0.58	1579	0.62	73.06	2.51	1.37	0.64
	nodular	5	1366	0.46	1574	2.36	87.34	1.82	1.61	0.82
2–3	non-granular	5	1368	0.62	1578	0.33	71.91	1.41	1.44	0.64
	granular	5	1366	1.02	1579	1.18	70.70	2.71	1.50	0.69
	nodular	6	1366	3.00	1577	1.74	80.25	5.37	1.77	0.79
2–4	non-granular	5	1367	0.85	1579	1.43	70.17	1.12	1.49	0.69
	granular	5	1363	1.07	1579	0.52	64.68	0.90	1.57	0.76
	nodular	5	1362	1.06	1579	2.46	71.82	5.83	1.77	0.84
2–6	non-granular	5	1363	0.98	1579	0.28	62.96	1.32	1.59	0.77
	granular	5	1362	1.87	1580	1.77	63.76	2.75	1.63	0.75
	nodular	5	1361	1.52	1580	1.57	71.95	1.70	1.86	0.89
2–7	non-granular	5	1362	1.26	1579	0.62	61.83	1.57	1.71	0.81
	granular	5	1362	0.82	1580	0.77	61.79	1.67	1.68	0.83
	nodular	4	1360	0.63	1580	0.77	69.27	1.57	2.01	0.91
2–8	non-granular	2	1362	0.64	1580	0.16	63.66	1.71	1.74	0.85
	granular	5	1361	2.09	1581	2.24	61.01	1.75	1.76	0.85
	nodular	5	1362	0.97	1581	0.92	64.39	3.33	2.10	0.96
2–9	non-granular	5	1363	1.30	1580	0.76	60.07	1.49	1.79	0.90
	granular	3	1363	0.38	1582	0.79	56.21	1.54	1.97	1.02
	nodular	3	1361	0.85	1582	0.19	62.04	0.27	2.14	1.12
2–11	non-granular	3	1363	1.55	1582	1.24	56.57	2.06	1.95	1.01
	granular	5	1360	0.46	1582	0.70	55.20	0.65	2.19	1.15
	nodular	5	1358	0.62	1583	1.00	59.14	1.09	2.33	1.18
2–12	non-granular	5	1360	0.79	1583	0.55	55.60	0.75	2.23	1.15
	granular	5	1353	2.37	1585	0.79	53.47	1.47	2.47	1.31
	nodular	5	1354	0.89	1585	0.66	56.50	1.20	2.50	1.36
2–13	non-granular	5	1356	0.77	1585	0.67	52.83	0.95	2.44	1.28

G-FWHM—full width at half maximum of the G peak; SD—standard deviation; n—number of measurements; A_{D1}/A_G—D1/G amplitude.

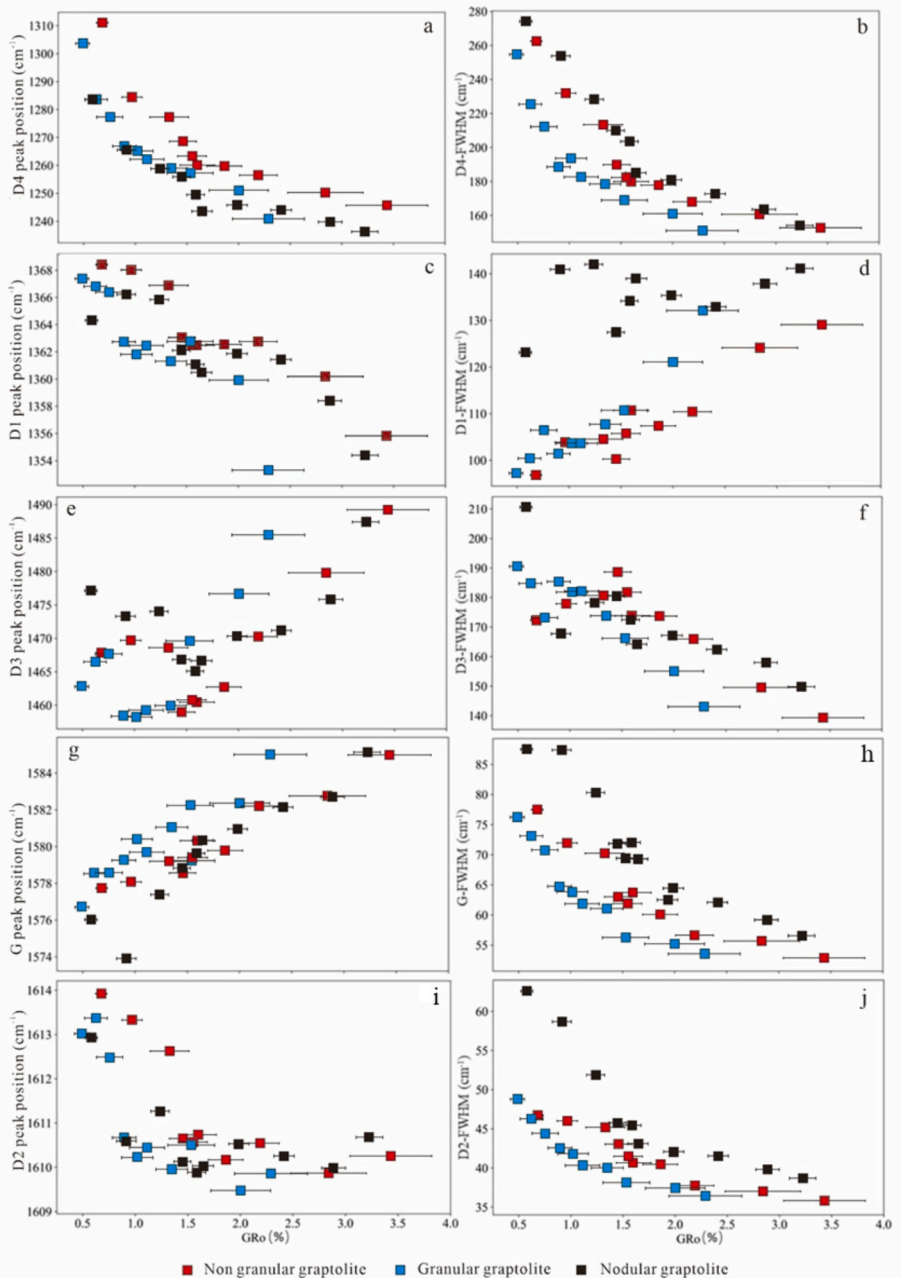

Fig. 4. The peak position and FWHM parameters of the five Raman band peaks (D4, D1, D3, G and D2) plotted as a function of graptolite reflectance (GR_o, in %). FWHM—full width at half maximum of the peak.

(either solid bitumen or bituminite). A nodular graptolite shows a dark ring of material around it (under white light), where the ring material is organic as well, with a slight compositional change (higher SE response) from the graptolite under SE (Fig. 5E), which might indicates that graptolitic epiderm, under pressure and temperature of 325C, exuded organic matter (typically aliphatic-alicyclic carbon, similar to vitrinite) during early carbonization (Goodarzi and Murchison, 1972; Goodarzi, 1985). This means graptolite is able to generate gaseous hydrocarbons at high maturity. There is a marked grayscale contrast between the graptolite and the surrounding solid bitumen in the SE 500× image (Fig. 6A). The difference in polishing relief is exhibited by a change in SE contrast, while elemental compositional changes can also be present under SE evaluation.

3.4. The development of mineral inclusions in graptolite

In Figs. 5E and 6C-F, fine-grained minerals are present within graptolite. The graptolite in Fig. 6 was identified as “non-granular graptolite” via optical microscopy observation. The fine-grained minerals found in some of the nodular graptolites (e.g., Fig. 5E) and the non-granular graptolite in samples 2–3, 2–4, 2–6, and 2–9 (e.g., Fig. 6) tend to be <200 nm in diameter, which is difficult to resolve at an optical magnification of 500×. The minerals in the granular graptolite tend to be larger (typically more than 400 nm in diameter), which would be easier to discern under the optical conditions used in this study. Also, note that there are zones in the graptolites that show an absence of granularity under SE (Fig. 5C-D, Fig. 6C-F) which may imply morphological differences in the original graptolite structure. Based on EDS analysis, there is a strong correlation of the fine-grained inclusions to Fe and S (Fig. 7A, B), while not much correlation between the grains and Si

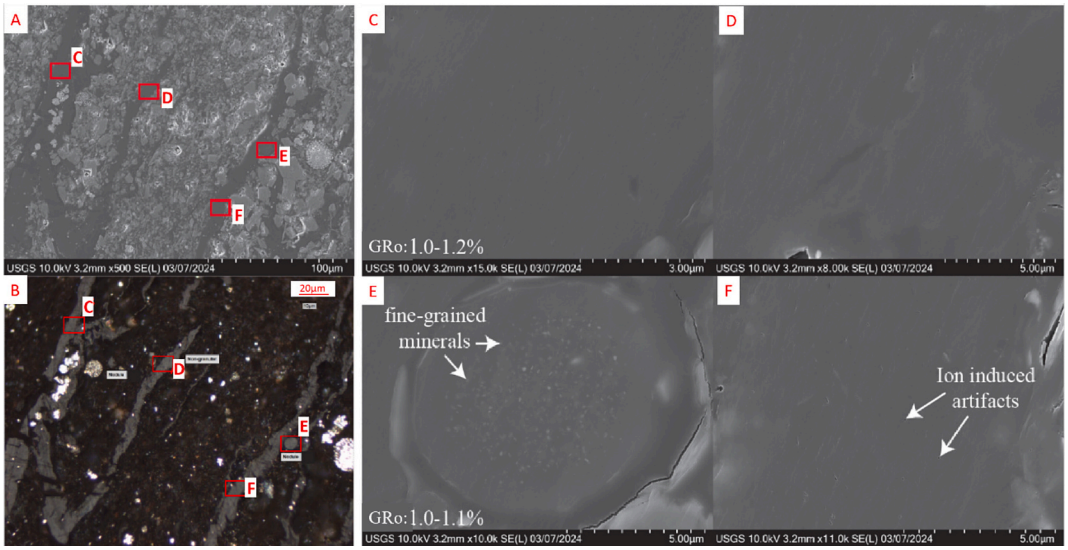

Fig. 5. Photomicrographs of an artificially matured (pyrolysis temperature: 325 °C, EASY%Ro: 0.85) lower Paleozoic graptolite-rich shale sample (sample 2–4). A) field emission scanning electron microscopy (FE-SEM) and B) Optical microscopy of non-granular and nodular graptolite showing locations of panels C-F; C), D), E), F) were collected under secondary electron (SE); there are clearly fine-grained minerals within the nodular graptolite (panel E). GR_o values labeled in panels C and E correspond to the specific region of interest. GR_o—mean random graptolite reflectance.

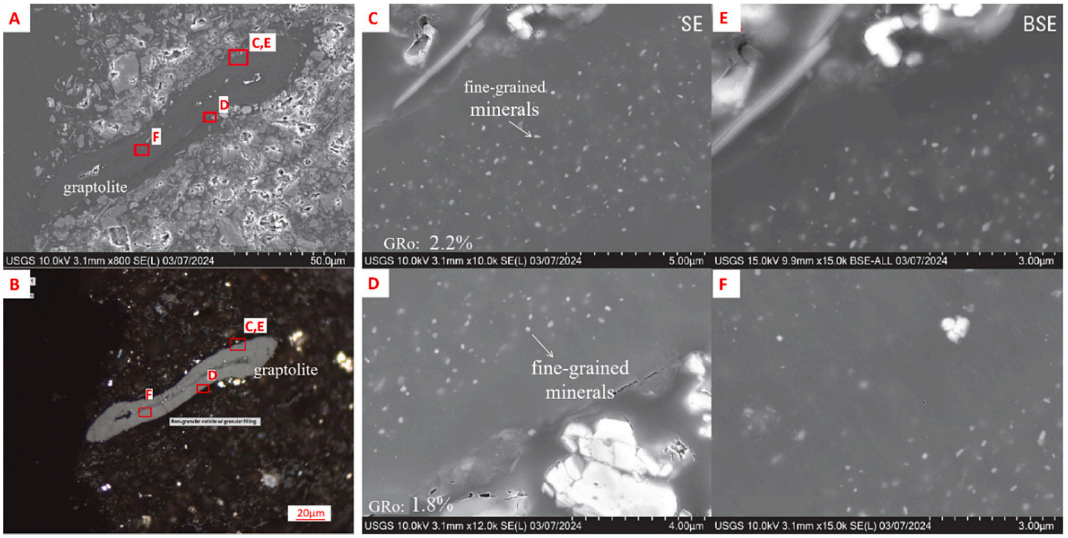

Fig. 6. Photomicrographs of an artificially matured (pyrolysis temperature: 415 °C, EASY%Ro: 2.0) lower Paleozoic graptolite-rich shale sample (sample 2–9). A) FE-SEM and B) Optical microscopy of the same non-granular graptolite showing locations of panels C-F; C), D), and F) were collected under SE, with fine-grained minerals clearly identified within the graptolite; E) is under BSE, there is marked grayscale contrast between the graptolite and the surrounding solid bitumen in the SE 500× image (panel A). GR_o values labeled in panels C and D correspond to the specific region of interest. GR_o—mean random graptolite reflectance.

(clay). Hence, the majority of the fine-grained material is interpreted as iron sulfide.

4. Discussion

4.1. Correlations between thermal maturity indicators

Commonly used Raman spectroscopy parameters D1, G-FWHM, and both D1 FWHM/G FWHM and D1/G amplitude (A_{D1}/A_G) ratios from this work are compared with those previously published data (Fig. 8) to discuss their utility in evaluating the thermal maturation of graptolites and how different environments and physiochemical difference may impact the Raman spectrum. As different laser wavelength and curve fitting methods can influence the peak position of each Raman band, only data generated from similar laser wavelength (532 nm) and 5-band curve fitting methods were compared in this work (Fig. 1). However, as the D1 band stays the same wavenumber once it is deconvoluted from 5-band or 4-band fittings, D1 band related parameters (Hao et al., 2019) were also added in this work for comparison.

The relationship between graptolite reflectance and D1-peak position from this work shows a generally similar evolution trend as previously reported data (Fig. 8a, Sauerer et al., 2017; Morga and Pawlyta, 2018; and Hao et al., 2019). Although all data were generated with a 532 nm laser, the D1-peak positions of this work are shifted toward lower wavenumbers relative to the data from Sauerer et al. (2017) and Hao et al. (2019) before entering the oil window stage of thermal maturation (Mukhopadhyay, 1994). However, there was a plateau observed in all the data from the GR_o value of 1 % to 2 %. At higher maturity, data from different works showed different evolution trends, among which the data distribution of natural samples and artificial

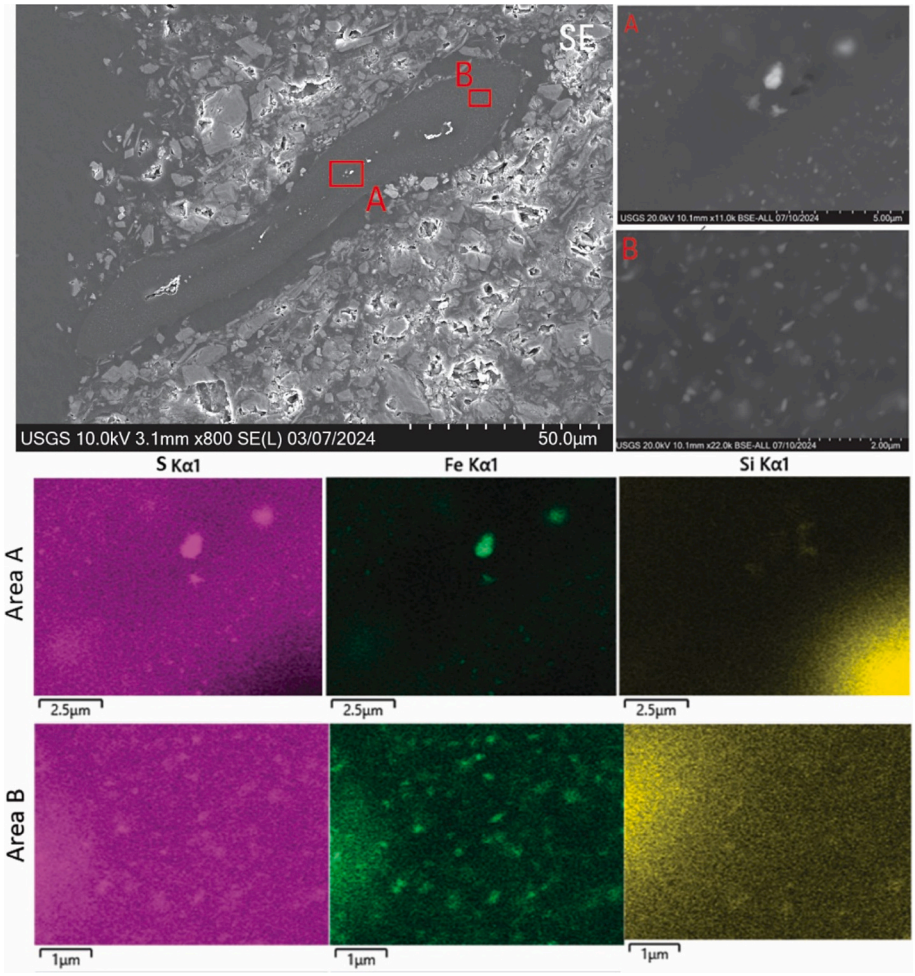

Fig. 7. Energy dispersive spectroscopy (EDS) analysis of an artificially matured (pyrolysis temperature: 415 °C, Easy%Ro: 2.0) lower Paleozoic graptolite-rich shale sample (sample 2–9): A) and B) are observed areas with different mineral inclusion abundance. Second and third row of image show the EDS maps of areas A and area B.

samples have different trends (Hao et al., 2019). This could be explained as the volatile hydrocarbon generated under experimental conditions, including aliphatic and alicyclic compounds, are retained within the system resulting in a decrease in viscosity, retardation of aromaticity, and suppression of the Ro (Goodarzi, 1985). As the D1 band is associated with the presence of disorder and defects in the carbon lattice, such as edges, grain boundaries and amorphous structure (Sauerer et al., 2017), the decrease of the D1 peak position with increasing GR_o could also be related to the expulsion of heteroatoms.

G-FWHM was compared with data from Sauerer et al. (2017) and Morga and Pawlyta (2018), showing conformity (Fig. 8b). However, as the Raman instrumentation set-up influences the absolute value (Henry et al., 2019), the peak position values of the G band from different works cannot be compared. The D1-FWHM /G-FWHM from this work matches the distribution of the D1-FWHM/G-FWHM from Sauerer et al. (2017), which was calculated based on the raw data (Hao et al., 2019, Fig. 8c), and supports the effectiveness of this parameter in assessing thermal maturity.

A_{D1}/A_G data measured from natural samples from Hao et al. (2019) and Sauerer et al. (2017) show continuing increase as thermal maturity increases. However, artificially matured samples from Hao et al. (2019) show a reverse trend after GR_o of 3.0 % (Fig. 7d). Although the data from this work shows a continuing increase, the rate of increase is lower compared to naturally matured samples from Hao et al. (2019) and Sauerer et al. (2017). This could be explained by the limited GR_o range examined. The different trends between naturally and artificially matured samples might be attributed to their differing molecular evolution pathways at a highly mature stage (GR_o of 2.0 %).What's more, as Hao et al. (2019) used block samples and anhydrous pyrolysis, the difference with data from this work could also be resulted from the physiochemical difference as the absence of water.

Besides, there was a downward shift in the peak intensity of D3 between 0.75 % and 1.5 % GR, which could be resulted from hydrocarbon generation and trapped within micropores. Baludikay et al. (2018) proposed that D3 band results from the out-of-plane vibration due to defects and heteroatoms, which eventually disappear during graphitization. Besides, D3 band from this work is a combination of D3 and D6 of the work from Romero-Sarmiento et al. (2014), of whom applied a 6-bands fitting. He proposed that D6 band to be related to hydrocarbon trapped within the micropores of organic matter (Romero-Sarmiento et al., 2014).

4.2. Mineral inclusions within graptolite

The abundance of mineral inclusions and their grain size differs among the three fractions of graptolite. In general, there are abundant "fine-grained" (<200 nm) minerals in the non-granular graptolite fraction compared to the granular fraction, which tends to have coarser (roughly >400 nm) but fewer inclusion grains. As the mineral inclusion grain size could impact surface polishing (thus impacting the overall reflectance), the non-granular graptolite with fine-grained mineral inclusions may develop a better polish compared to the fewer, larger

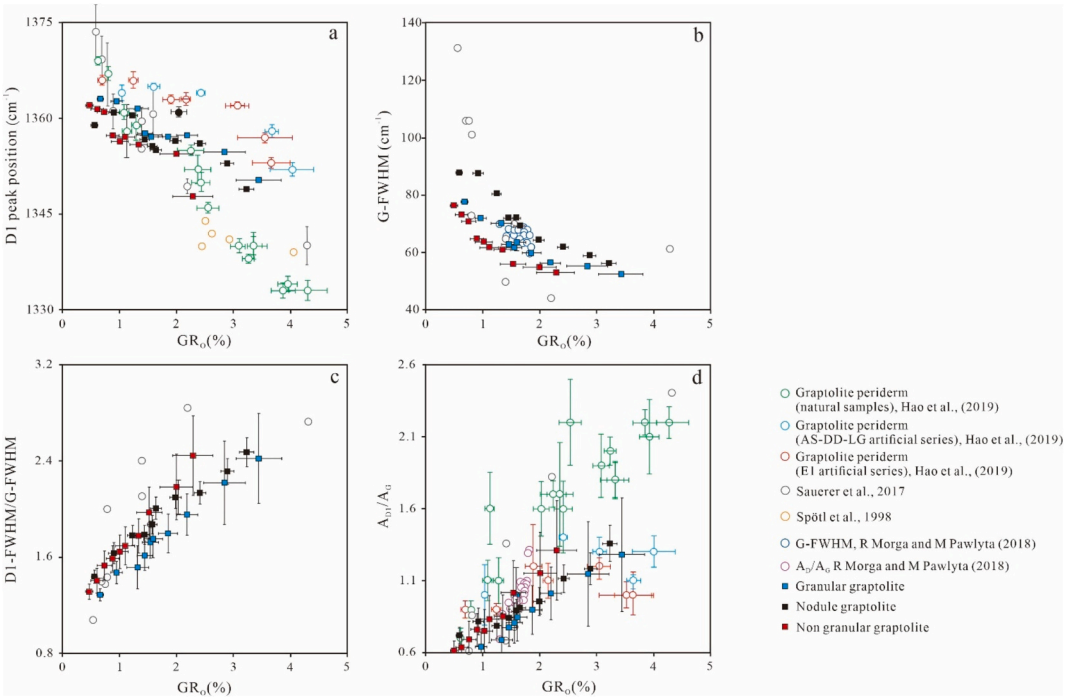

Fig. 8. Evolution of common Raman spectral parameters D1-peak position, G-FWHM, $D1_{FWHM}/G_{FWHM}$ and A_{D1}/A_G in this work and in previous work with respect to graptolite reflectance (GR_o). a) GR_o vs D1-peak position; b) GR_o vs G-FWHM; c) GR_o vs D-FWHM/G-FWHM; d) GR_o vs A_D/A_G (data from Morga and Pawlyta, 2018; and Hao et al., 2019). G-FWHM—full width at half maximum of the G peak; D1-FWHM—full width at half maximum of the D1 peak; A_{D1}/A_G—D1/G amplitude.

minerals grains in the granular fraction, thus impacting the overall reflectance as documented in Table 1, e.g., non-granular graptolite has systematically higher reflectance than co-occurring granular graptolite. Minerals associated with graptolite also are found in other works, e.g., Ma et al. (2016) reported mineral grains developed in the cortical bandages of graptolite periderm in Wufeng-Longmaxi shale. Underwood (1992) proposed that the skeleton of graptolites could provide a locus for the precipitation of authigenic mineral formation.

4.3. Bireflectance of graptolite

Bireflectance is the most informative optical properties of OMs. It is indicative of the degree of ordering of the molecular structure of OMs, and for OMs with uniaxial negative indicatrix (vitrinite, graptolite) is determined using the maximum in section parallel to the bedding and the minimum reflectance in section perpendicular to bedding (Goodarzi and Murchison, 1972; Goodarzi et al., 2024b). Graptolite bireflectance arises from the anisotropy of differing crystallographic axes, revealing the degree of molecular orientation and ordering, and is crucial for determining crystallographic effects in OM. Our data showed that bireflectance has little increase as a function of EASY%Ro for the nodular graptolite fraction, but a marked increase for the non-granular and granular graptolite fractions (Fig. 9). Similarly, D1-FWHM for the nodular graptolite fraction, which illustrates the degree of disorder, does not change much in the nodular population across the thermal maturity range of this study (Fig. 4d). This might suggest that there is an anisotropic nature to the aromatic structure that is captured by the D1 results of the nodular graptolite dataset, where disorder is apparently constant with increasing GR_o when looking down the axis of the graptolite body, but increases when measured on the in-plane orientation.

4.4. The effect of pyrite on thermal maturation evolution of graptolite

The continuous reflectance evolution trend of the three graptolite fractions from the same sample set (Zheng et al., 2022, Fig. S1) shows different increases in coefficient, among which the non-granular

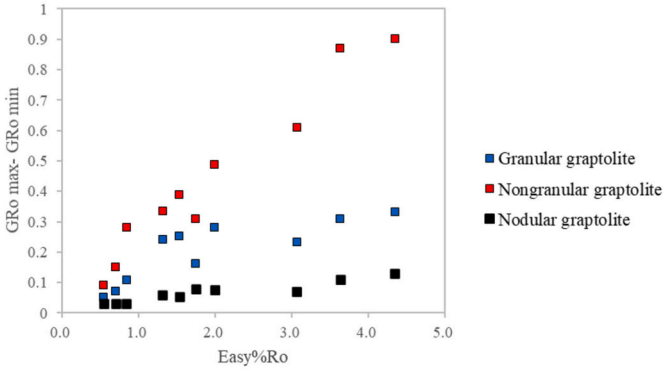

Fig. 9. The relationship between bireflectance and EASY%Ro for the nodular, non-granular, and granular graptolite types of artificially matured samples from immature to metagenesis window (data from Zheng et al., 2022 and shown in Table. 1S).

graptolites have the greatest slope while the granular graptolites have the shallowest slope. This may suggest that granular graptolite has a lower maturation rate, which might be related to catalysis induced by pyrite inclusions. However, Hatcherian et al. (2023) conducted a series of hydrous pyrolysis experiments at varying temperatures and pyrite abundances, and found that solid bitumen reflectance was higher in residues with greater pyrite concentrations at relatively lower pyrolysis temperature (< 350 °C). Moreover, their samples with the highest pyrite abundance had the lowest hydrogen index (HI) and programmed pyrolysis T_{max} values regardless of pyrolysis temperature. Lower T_{max} was interpreted as caused by oil carryover and lower HI was interpreted as indicative of enhanced maturation (Yang and Horsfield, 2020). These extant results may suggest that the higher maturation rate in non-granular graptolite observed by Zheng et al. (2022) is induced through catalysis caused by abundant fine-grained pyrite inclusions (<200 nm, not resolvable with optical microscopy), whereas fewer

(although larger, e.g., >400 nm) sulfide inclusions in granular graptolite do not influence maturation, but instead contribute to polishing defects which result in lower GR_o (e.g., Hackley et al., 2018). Li et al. (2022) compared the hydrocarbon generation of pyrite-containing and pyrite-removed kerogen and suggested that inherent pyrite accelerates the generation of liquid hydrocarbons, and that the yield of bitumen/heavy hydrocarbons (C_{14+}) was lower in the kerogen containing pyrite due to strong bonding interactions between pyrite and kerogen. However, as their work was conducted through anhydrous pyrolysis, the role of water was not considered.

4.5. The effect of supercritical water on graptolite

There are suppressed GR_o versus VR_o slopes (around 60 %) observed after VR_o of 1.12–1.25 %, which corresponds to hydrous pyrolysis temperatures of 350–370 °C (Zheng et al., 2022, Fig. S1). The deionized water added in the gold tube could also contribute to this phenomenon. Water becomes supercritical when reaching the critical point (374 °C and 22.1 MPa), where it has liquid-like density with gas-like diffusivity, viscosity, and unique solvent properties (Weingärtner and Franck, 2005). Hence, its reaction mechanism and effect on OM differ from vapor or liquid water. Barker and Lewan (1999) observed a retardation in VR_o increase with increasing temperature in supercritical water pyrolysis. This could be attributed to molecular disorder increases (Khorasani et al., 1990) and fluctuations in the fraction of aromatic carbon within the zone of reduced VR_o (Goodarzi and Murchison, 1972; Barker et al., 1996), which could be supported by the plateau in the trend between D-peak position (wavelength range: 1355–1360 cm^{-1}) and GR_o in the range of 1 % to 2 % in this work (Fig. 8a), as the D band is associated with the presence of disorder and defects in the carbon lattice (Sauerer et al., 2017).

5. Conclusion

This study addresses the challenges and complexities of evaluating the thermal maturity of graptolite in lower Paleozoic sediments by employing gold tube hydrous pyrolysis to artificially mature a graptolite-rich Alum Shale sample followed by correlated Raman spectral measurements, organic petrology and FE-SEM observations. The results indicates that:

(1) The three types of non-granular, granular, and nodular graptolite periderm have molecular and structural variability, which reflected on their thermal maturity trends.
(2) The non-granular graptolite showing clear Raman spectral shifts and FWHM trends indicative of increasing aromaticity and structural ordering.
(3) A comparison between Raman data from this work and data from previous studies showed different evolution trends between natural samples and artificially matured samples with equivalent reflectance. Indicating of the is a very sensitive and useful method for assesses thermal maturity of the three types of graptolite.
(4) The bireflectance of all artificially matured three types of graptolite epiderms increases continuously with increasing of temperature. However, bireflectance of the nodular graptolite shows the least and the non-granular graptolite show a sharp increase with increasing temperature. However, the granular graptolite maintaining a trend between the nodular graptolite and the non-granular graptolite, indicating the greatest ordering of molecular structural changes occurred in the in non-granular and least in nodular graptolite.
(5) The combining optical microscopy, Raman spectroscopy, and FE-SEM, provide a better understanding molecular structural changes during thermal treatment and maturity.
(6) Mineral inclusions in graptolite epiderms includes fine-grained (~100–200) in non-granular graptolite and nodular graptolite, and coarse-grained (~300–1400 nm) in granular graptolite, and their presences did not influence the maturity of the sample.

CRediT authorship contribution statement

Xiaowei Zheng: Writing – review & editing, Writing – original draft, Investigation, Funding acquisition, Data curation, Conceptualization. **Hamed Sanei:** Supervision, Investigation. **Fujie Jiang:** Supervision, Investigation. **Qingyong Luo:** Writing – review & editing. **Ye Wang:** Writing – original draft, Investigation. **Jennifer L. Nedzweckas:** Writing – original draft, Methodology, Investigation, Data curation. **Brett J. Valentine:** Writing – original draft, Methodology, Investigation, Data curation. **M. Rebecca Stokes:** Writing – original draft, Methodology, Investigation, Data curation. **Liu Cao:** Visualization. **Paul C. Hackley:** Writing – review & editing, Writing – original draft, Supervision, Investigation, Data curation.

Declaration of competing interest

The authors declare that they have no known competing financial interests or personal relationships that could have appeared to influence the work reported in this paper.

Acknowledgements

Reviews by Denise Levitan and Palma J. Botterell (U.S. Geological Survey, USGS) improved the manuscript. The original immature Alum Shale sample was provided by Dr. Niels H. Schovsbo. Yuan Li and Jingqi Zhou from College of Geosciences, China University of Petroleum, Beijing are thanked for their assistance in visualization. This research was financially supported by the lower Paleozoic Consortium from the LOC laboratory, Aarhus University and the China University of Petroleum, Beijing. Xiaowei Zheng was supported by the start-up funding from China University of Petroleum, Beijing (2462024BJRC007) and the National Natural Science Foundation of China (No. 42402149). Qingyong Luo was supported by National Natural Science Foundation of China (No. 42122016). All USGS-generated data from this study is available online from Zheng et al. (2025) https://doi.org/10.5066/P1FOPMCI in a data release created by Jeremy Ray (USGS). This work was supported by the Energy Resources Program of the USGS. Any use of trade, firm, or product names is for descriptive purposes only and does not imply endorsement by the U.S. Government.

Appendix A. Supplementary data

Supplementary data to this article can be found online at https://doi.org/10.1016/j.coal.2025.104793.

Data availability

I have shared the link to my data at the acknowledgement.

References

Baludikay, B.K., François, C., Sforna, M.C., Beghin, Jérémie, Cornet, Y., Storme, J.Y., 2018. Raman microspectroscopy, bitumen reflectance and illite crystallinity scale: comparison of different geothermometry methods on fossiliferous proterozoic sedimentary basins (dr Congo, Mauritania and Australia). Int. J. Coal Geol. 191, 80–94.
Barker, C.E., Lewan, M.D., 1999, March. The effect of supercritical water on vitrinite reflectance as observed in contact metamorphism and pyrolysis experiments. In: Abstracts of Papers of the American Chemical Society, 217. AMER CHEMICAL SOC, 1155 16TH ST, NW, WASHINGTON, DC 20036 USA pp. U822-U822.
Barker, C.E., Lewan, M.D., Pawlewicz, M.J., 1996. A Simple Hydrous Pyrolysis Technique to Detect Suppressed Vitrinite Reflectance.
Bertrand, R., 1990. Correlations among the reflectances of vitrinite, chitinozoans, graptolites and scolecodonts. Org. Geochem. 15 (6), 565–574.

Beyssac, O., Goffé, B., Chopin, C., Rouzaud, J.N., 2002. Raman spectra of carbonaceous material in metasediments: a new geothermometer. J. Metamorph. Geol. 20, 859–871.
Bustin, R.M., Link, C., Goodarzi, F., 1989. Optical properties and chemistry of graptolite periderm following laboratory simulated maturation. Org. Geochm. 14 (4), 355–364.
Ferralis, N., Matys, E.D., Knoll, A.H., Hallmann, C., Summons, R.E., 2016. Rapid, direct and non-destructive assessment of fossil organic matter via microRaman spectroscopy. Carbon 108, 440–449.
Goodarzi, F., 1984. Organic petrography of graptolite fragments from Turkey. Mar. Pet. Geol. 1 (3), 202–210.
Goodarzi, F., 1985. Optical properties of vitrinite carbonised under pressure. Fuel 64, 158162.
Goodarzi, F., Murchison, D.G., 1972. Optical properties of carbonised vitrinites. Fuel 51, 322328.
Goodarzi, F., Norford, B.S., 1987. Optical properties of Graptolite Epiderm-a Review. Bull. Geol. Soc. Den. 35, 141–147.
Goodarzi, F., Hosseininejad, S., Pedersen, P.K., Gentzis, T., Sanei, H., 2022. Characterization of immature oil shales from the Cretaceous Second White Specks Formation in Saskatchewan and Manitoba, Canada Marine. Pet. Geol. 143 (105774).
Goodarzi, F., Gentzis, T., Luo, Q., Sanei, H., 2024. Bituminite-Bitumen-Migra Bitumen. In: Borrego, A.G. (Ed.), The 75th ICCP Meeting. A Commemorative Book. Instituto de Ciencia y Tecnología del Carbono (INCAR-CSIC), Oviedo, Spain, pp. 109–123. ISBN: 978-84-09-64254-0.
Goodarzi, F., Gentzis, T., Luo, Q., Sanei, H., Bian, L., Norford, B., 2024b. Influence of geology on the thermal maturity of graptolite-A review. In: Borrego, A.G. (Ed.), The 75th ICCP Meeting. A Commemorative Book. Instituto de Ciencia y Tecnología del Carbono (INCAR-CSIC), Oviedo, Spain p.125–14. ISBN: 978-84-09-64254-0.
Hackley, P.C., Lünsdorf, N.K., 2018. Application of Raman spectroscopy as thermal maturity probe in shale petroleum systems: insights from natural and artificial maturation sequences. Energy Fuel 32, 11190–11202.
Hackley, P.C., Valentine, B.J., Hatcherian, J.J., 2018. On the petrographic distinction of bituminite from solid bitumen in immature to early mature source rocks. Int. J. Coal Geol. 196, 232–245.
Hao, J., Zhong, N., Luo, Q., Liu, D., Wu, J., Liu, A., 2019. Raman spectroscopy of graptolite periderm and its potential as an organic maturity indicator for the Lower Paleozoic in southwestern China. Int. J. Coal Geol. 213, 103278.
Hatcherian, J., Adsul, T., Hackley, P., Ghosh, S., Varma, A.K., 2023. Impact of pyrite-sourced sulfur on catagenesis in gilsonite undergoing hydrous pyrolysis. Bull. Geol. Soc. Greece.
Henry, D.G., Jarvis, I., Gillmore, G., Stephenson, M., Emmings, J.F., 2018. Assessing low-maturity organic matter in shales using Raman spectroscopy: effects of sample preparation and operating procedure. Int. J. Coal Geol. 191, 135–151.
Henry, D.G., Jarvis, I., Gillmore, G., Stephenson, M., 2019. Raman spectroscopy as a tool to determine the thermal maturity of organic matter: application to sedimentary, metamorphic and structural geology. Earth Sci. Rev. 198, 102936.
ICCP, 1998. The new vitrinite classification (ICCP System 1994). Fuel 77 (5), 349–358.
Jin, X., Wu, J., Silva, R.C., Huang, H., Zhang, Z., Zhong, N., Tutolo, B.M., Larter, S., 2021. Alternate routes to sustainable energy recovery from fossil fuels reservoirs. Part 1. Investigation of high-temperature reactions between sulfur oxy anions and crude oil. Fuel 302, 121050.
Jubb, A.M., Botterell, P.J., Birdwell, J.E., Burruss, R.C., Hackley, P.C., Valentine, B.J., Hatcherian, J.J., Wilson, S.A., 2018. High microscale variability in Raman thermal maturity estimates from shale organic matter. Int. J. Coal Geol. 199, 1–9.
Kelemen, S.R., Fang, H.L., 2001. Maturity trends in Raman spectra from kerogen and coal. Energy Fuel 15, 653–658.
Khorasani, G.K., Murchison, D.G., Raymond, A.C., 1990. Molecular disordering in natural cokes approaching dyke and sill contacts. Fuel 69 (8), 1037–1046.
Li, K., Zhao, Z., Lu, H., Liu, X., Peng, P.A., Hsu, C.S., 2022. Effects of inherent pyrite on hydrocarbon generation by thermal pyrolysis: An example of low maturity type-II kerogen from Alum shale formation, Sweden. Fuel 312, 122865.
Link, C.M., Bustin, R.M., Goodarzi, F., 1990. Petrology of graptolites and their utility as indices of thermal maturity in Lower Paleozoic strata in northern Yukon, Canada. Int. J. Coal Geol. 15 (2), 113–135.
Liu, D., Xiao, X., Tian, H., Min, Y., Zhou, Q., Cheng, P., Shen, J., 2013. Sample maturation calculated using Raman spectroscopic parameters for solid organics: methodology and geological applications. Chin. Sci. Bull. 58, 1285–1298. https://doi.org/10.1007/s11434-012-5535-y.
Luo, Q., Hao, J., Skovsted, C.B., Luo, P., Khan, I., Wu, J., Zhong, N., 2017. The organic petrology of graptolites and maturity assessment of the Wufeng–Longmaxi Formations from Chongqing, China: Insights from reflectance cross-plot analysis. Int. J. Coal Gel. 183, 161–173.
Luo, Q., Hao, J., Skovsted, C.B., Xu, Y., Liu, Y., Wu, J., Zhang, S., Wang, W., 2018. Optical characteristics of graptolite-bearing sediments and its implication for thermal maturity assessment. Int. J. Coal Geol. 195, 386–401.
Ma, Y., Zhong, N., Cheng, L., Pan, Z., Dai, N., Zhang, Y., Yang, L., 2016. Pore structure of the graptolite-derived OM in the Longmaxi Shale, southeastern Upper Yangtze Region, China. Mar. Pet. Geol. 72, 1–11.
Marshall, A.O., Wehrbein, R.L., Lieberman, B.S., Marshall, C.P., 2012. Raman spectroscopic investigations of burgess shale-type preservation: a new way forward. Palaios 27, 288–292.
Morga, R., Pawlyta, M., 2018. Microstructure of graptolite periderm in Silurian gas shales of Northern Poland. Int. J. Coal Geol. 189, 1–7.
Mukhopadhyay, P.K., 1994. Vitrinite reflectance as maturity parameter: Petrographic and molecular characterization and its applications to basin modeling. In: Mukhopadhyay, P.K., Dow, W.G. (Eds.), Vitrinite Reflectance as a Maturity Parameter: Applications and Limitations, vol. 570. American Chemical Society Symposium Series, Washington, D.C, pp. 1–24.
Mumm, A.S., İnan, S., 2016. Microscale organic maturity determination of graptolites using Raman spectroscopy. Int. J. Coal Geol. 162, 96–107.
Petersen, H.I., Schovsbo, N.H., Nielsen, A.T., 2013. Reflectance measurements of zooclasts and solid bitumen in lower Palaeozoic shales, southern Scandinavia: correlation to vitrinite reflectance. Int. J. Coal Geol. 114, 1–18.
Reyes, J., Jiang, C., Lavoie, D., Armstrong, D.K., Milovic, M., Robinson, R., 2018. Organic petrographic analysis of artificially matured chitinozoan-and graptolite-rich Upper Ordovician shale from Hudson Bay Basin, Canada. Int. J. Coal Geol. 199, 138–151.
Riediger, C., Goodarzi, F., 1989. Graptolites as indicators of regional maturity in lower Paleozoic sediments, Selwyn Basin, Yukon and Northwest Territories, Canada. Can. J. Earth Sci. 26 (10), 2003–2015.
Romero-Sarmiento, M.F., Rouzaud, J.N., Bernard, S., Deldicque, D., Thomas, M., Littke, R., 2014. Evolution of Barnett shale organic carbon structure and nanostructure with increasing maturation. Org. Geochem. 71, 7–16.
Sauerer, B., Craddock, P.R., AlJohani, M.D., Alsamadony, K.L., Abdallah, W., 2017. Fast and accurate shale maturity determination by Raman spectroscopy measurement with minimal sample preparation. Int. J. Coal Geol. 173, 150–157.
Stokes, M.R., Valentine, B.J., Hackley, P.C., Jubb, A.M., 2022. Relating systematic compositional variability to the textural occurrence of solid bitumen in shales. Int. J. Coal Geol. 261, 104068.
Suárez-Ruiz, I., Flores, D., Mendonca Filho, J.G., Hackley, P.C., 2012. Review and update of the applications of organic petrology: part 1, geological applications. Int. J. Coal Geol. 99, 54–112.
Sweeney, J.J., Burnham, A.K., 1990. Evaluation of a simple model of vitrinite reflectance based on chemical kinetics. AAPG Bull. 74 (10), 1559–1570.
Teichmüller, M., Teichmüller, R., 1979. Diagenesis of coal (coalification). In: Developments in sedimentology, Vol. 25. Elsevier, pp. 207–246.
Tuinstra, F., Koenig, J.L., 1970. Raman spectrum of graphite. J. Chem. Phys. 53, 1126–1130.
Underwood, C.J., 1992. Graptolite preservation and deformation. Palaios 178–186.
Valentine, B.J., Hackley, P.C., 2023. Scanning electron microscopic evaluation of broad ion beam milling effects to sedimentary organic matter: sputter-induced artifacts or naturally occurring porosity? Int. J. Coal Geol. 277, 104348.
Valentine, B.J., Hackley, P.C., Hatcherian, J., Yu, J.-J., 2019. Reflectance increase from broad beam ion milling of coals and organic-rich shales due to increased surface flatness. Int. J. Coal Geol. 201, 86–101.
Weingärtner, H., Franck, E.U., 2005. Supercritical water as a solvent. Angew. Chem. Int. Ed. 44 (18), 2672–2692.
Wilkins, R.W.T., Boudou, R., Sherwood, N., Xiao, X., 2014. Thermal maturity evaluation from inertinites by Raman spectroscopy: the 'RaMM' technique. Int. J. Coal Geol. 128-129, 143–152.
Wu, J., Qi, W., Jiang, F.J., Luo, Q.Y., Zhang, C.L., Hu, H.Z., Wang, Z., Ma, Q.S., Tang, Y. C., 2021. Influence of sulfate on the generation of bitumen components from kerogen decomposition during catagenesis. Pet. Sci. 18, 1611–1618.
Wu, T., Lu, C., Sun, T., Li, Y., 2022. Study on Raman multi-peak fitting and structure quantitative analysis of PAN-based carbon fibers. J. Mater. Sci. 57 (32), 15385–15412.
Zheng, X., Sanei, H., Schovsbo, N.H., Luo, Q., Wu, J., Zhong, N., Galloway, J.M., Goodarzi, F., 2021. Role of zooclasts in the kerogen type and hydrocarbon potential of the lower Paleozoic Alum Shale. Int. J. Coal Geol. 248, 103865.
Zheng, X., Schovsbo, N.H., Luo, Q., Wu, J., Zhong, N., Goodarzi, F., Sanei, H., 2022. Graptolite reflectance anomaly. Int. J. Coal Geol. 261, 104072.
Yang, S., Horsfield, B., 2020. Critical review of the uncertainty of Tmax in revealing the thermal maturity of organic matter in sedimentary rocks. Int. J. Coal Gel. 225, 103500.
Zheng, X., Sanei, H., Jiang, F., Luo, Q., Wang, Y., Nedzweckas, J.L., Valentine, B.J., Stokes, M.R., Cao, L., Hackley, P.C., 2025. Raman spectral parameters of pyrolyzed samples for three types of graptolites. In: U.S. Geological Survey Data Release.